

Controlled Synthesis of a Two-Dimensional Non-van der Waals Ferromagnet toward a Magnetic Moiré Superlattice

Zhitong Jin,[‡] Zijie Ji,[‡] Yunlei Zhong, Yunmin Jin, Xianyu Hu, Xingxing Zhang, Lijing Zhu, Xianhui Huang, Tao Li, Xinghan Cai,* and Lin Zhou*



Cite This: *ACS Nano* 2022, 16, 7572–7579



Read Online

ACCESS |

Metrics & More

Article Recommendations

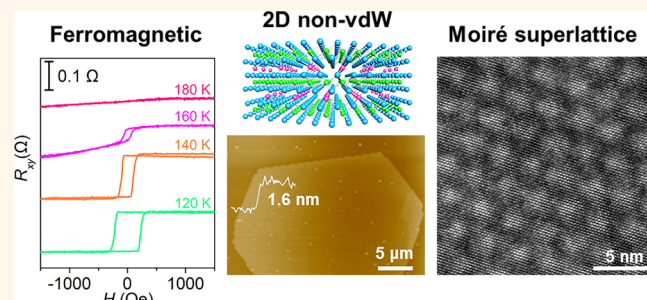
Supporting Information

ABSTRACT: Two-dimensional (2D) magnetic materials provide an ideal platform for spintronics, magnetoelectrics, and numerous intriguing physical phenomena in 2D limits. Moiré superlattices based on 2D magnets offer an avenue for controlling the spin degree of freedom and engineering magnetic properties. However, the synthesis of high-quality, large-grain, and stable 2D magnets, much less obtaining a magnetic moiré superlattice, is still challenging. We synthesize 2D ferromagnets (trigonal Cr₅Te₈) with controlled thickness and robust stability through chemical vapor deposition. Single-unit-cell-thick flakes with lateral sizes of tens of micrometers are obtained. We observe the layer-by-layer growth mode for the crystal formation in non-van der Waals Cr₅Te₈. The robust anomalous Hall signal confirms that Cr₅Te₈ of varying thickness have a long-range ferromagnetic order with an out-of-plane easy axis. There is no obvious change of the Curie temperature when the thickness of Cr₅Te₈ decreases from 52.1 to 7.2 nm. Here, we construct diverse 2D non-van der Waals/van der Waals vertical heterostructures (Cr₅Te₈/graphene, Cr₅Te₈/h-BN, Cr₅Te₈/MoS₂). A uniform moiré superlattice is formed in the heterostructure through a lattice mismatch. The successful growth of 2D Cr₅Te₈ and a related moiré superlattice introduces 2D non-van der Waals ferromagnets into moiré superlattice research, thus highlighting prospects for property investigation of a non-van der Waals magnetic moiré superlattice and massive applications which require a scalable approach to magnetic moiré superlattices.

KEYWORDS: chemical vapor deposition, moiré superlattice, 2D ferromagnet, Cr₅Te₈, non van der Waals

A moiré superlattice formed by two-dimensional (2D) layers modulates the crystal's periodicity and provides a tunable platform to investigate strong electron correlations and topological phases.^{1–4} Numerous exciting phenomena have been uncovered in graphene and non-magnetic transition-metal dichalcogenide based moiré superlattices, such as superconductivity,⁵ Mott insulator states,⁶ orbital magnetism,⁷ moiré excitons,⁸ and Wigner crystal state.⁹ Theoretical works predict moiré superlattice can also control the spin degree of freedom and engineer magnetic properties by introducing a 2D magnetic layer into the superlattice,^{10–12} but moiré superlattice involved 2D magnets are experimentally scarce.^{13,14}

Two-dimensional (2D) crystals with layered magnetism give access to diverse exciting physical phenomena and massive technologies.^{15–21} So far, most explored 2D magnets have van der Waals (vdW) structures, such as CrI₃, CrBr₃, and Fe₃GeTe₂, and are unstable under ambient or postprocess conditions. The vdW crystals occupy a small proportion of



crystal materials (~5%),²² but most 2D magnets works are restricted in 2D vdW magnets.^{15–19,23–27} In contrast, numerous non-van der Waals (non-vdW) magnets with desirable properties (ferromagnetism with high Curie temperature, stable, etc.) are rarely investigated in their 2D form. 2D non-vdW magnets provide a tremendous number of materials for property investigation, regulating magnetic and electrical properties, and fabricating nanoscale spintronic devices.²⁸ However, research on 2D non-vdW magnets is still in its infancy.^{29–33} The main hindrance to studying 2D non-vdW magnets and integrating them into a moiré superlattice is

Received: December 11, 2021

Accepted: April 14, 2022

Published: April 20, 2022



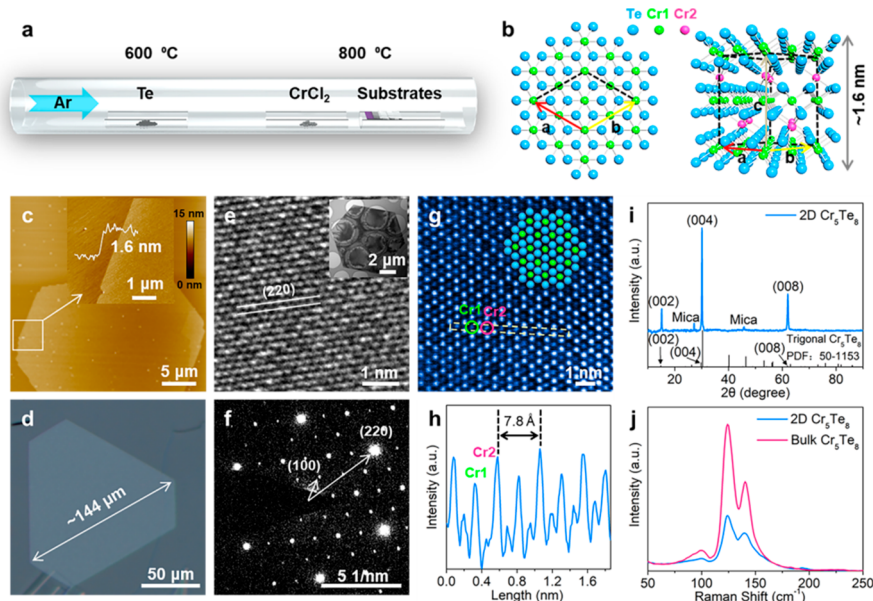


Figure 1. Synthesis and characterization of CVD-grown Cr_5Te_8 flakes. (a) Schematic illustration of the CVD setup for the growth of ultrathin Cr_5Te_8 flakes on stacked SiO_2/Si substrate and mica. (b) Atomic structure (top and side views) of the trigonal Cr_5Te_8 . Blue spheres denote tellurium atoms; green and red spheres denote two types of chromium atoms. (c) AFM image of a single unit cell thick Cr_5Te_8 flake on mica substrate. (d) Typical OM image of thin Cr_5Te_8 single crystal. (e, f) Low-magnification TEM image (inset), high-resolution TEM image (e), and corresponding SAED pattern (f) of the Cr_5Te_8 flake. (g) Atomic-resolution HAADF-STEM image of Cr_5Te_8 flake. Blue spheres denote tellurium atoms, and green spheres represent chromium atoms. (h) Intensity line profile along the yellow dashed square in (g). (i) XRD spectra of as-grown Cr_5Te_8 on a quartz substrate. (j) Raman spectra of 2D Cr_5Te_8 flake and bulk trigonal Cr_5Te_8 crystal.

obtaining high-quality, large-grain 2D non-vdW magnetic crystals. In particular, as a counterpart of monolayer for vdW materials, large-grain single-unit-cell-thick non-vdW materials are in high demand for moiré superlattices but are rare.

Here, we synthesize the high-quality 2D non-vdW magnet Cr_5Te_8 with tunable thickness via chemical vapor deposition (CVD). We obtain an atomically thin Cr_5Te_8 flake a single unit cell thick, with a lateral size of tens of micrometers. Thicker Cr_5Te_8 flakes with a submillimeter single-crystal grain are grown by controlling the growth time. Cr_5Te_8 flakes with varying thicknesses show metallic and ferromagnetic properties. The Curie temperature of Cr_5Te_8 shows no noticeable change when its thickness is decreased. Notably, Cr_5Te_8 flakes manifest robust stability in the aging and deterioration test. The scalable growth of chemically stable ferromagnet Cr_5Te_8 offers an excellent candidate for myriad applications of 2D ferromagnets.

More significantly, we observe that the growth of 2D non-vdW Cr_5Te_8 follows a layer-by-layer style and construct a 2D magnetic moiré superlattice. The large-grain ultimately thin Cr_5Te_8 flake in conjunction with layer-by-layer growth ensure the as-grown Cr_5Te_8 has a continuous layer structure instead of discrete islands. We grow the 2D non-vdW Cr_5Te_8 on diverse vdW materials and form magnetic vdW heterostructures ($\text{Cr}_5\text{Te}_8/\text{graphene}$, $\text{Cr}_5\text{Te}_8/\text{h-BN}$, $\text{Cr}_5\text{Te}_8/\text{MoS}_2$). A moiré superlattice forms in the 2D magnetic non-vdW/vdW heterostructure through a lattice mismatch. The superlattice is uniform and highly ordered without lattice distortion. Our finding enlarges the materials library of 2D magnetic moiré superlattices and provides a scalable approach to integrate 2D non-vdW magnets into a moiré superlattice. We envisage that the work offers platforms for investigating low-dimensional magnetic phenomena and directions for scalable constructing moiré superlattices.

RESULTS

2D Cr_5Te_8 flakes are synthesized using a home-built CVD setup. We choose CrCl_2 and Te as precursors to synthesize Cr_5Te_8 . Mica and SiO_2/Si are used as growth substrates (Figure 1a), and 200 sccm pure argon is utilized as the carrier gas. The growth temperature of the substrate is kept at 800 °C (Figure 1a, see details in the Methods). A typical optical microscopy (OM) image shows as-grown Cr_5Te_8 flakes on mica and SiO_2/Si substrates with truncated triangular or hexagonal shapes (Figure S1a,b). Trigonal Cr_5Te_8 has a five-layer superstructure of the CdI_2 type ($P\bar{3}m1$ space group) with lattice parameters $a = b = 7.82 \text{ \AA}$ and $c = 11.99 \text{ \AA}$.^{34,35} The nonlayer structure reveals that the trigonal Cr_5Te_8 is a non-vdW material (Figure 1b). Considering the adjacent top and bottom Te atom layers, the thickness of a single unit cell Cr_5Te_8 flake is around 1.6 nm. The thinnest flake is ~1.6 nm thick (lateral size ~30 μm), corresponding to a single unit cell of Cr_5Te_8 (Figure 1c, Figure S1c,d). The thickness and grain size strongly depend on the growth time and gradually increase as the growth time is prolonged (Figure S2). Representative atomic force microscope (AFM) images of individual Cr_5Te_8 flakes with different thicknesses are displayed in Figure S3. The grain sizes of single Cr_5Te_8 flakes are up to sub-millimeter (~144 and ~200 μm for thin and thick flakes in Figure 1d, Figure S2f), revealing large-grain 2D Cr_5Te_8 can be synthesized using our method.

Since chromium telluride has several crystalline phases, we carefully verify the crystalline structures of CVD-grown samples via transmission electron microscopy (TEM), electron dispersive spectroscopy (EDS), and high-angle annular dark-field scanning transmission electron microscopy (HAADF-STEM). Representative high-resolution transmission electron microscopy (HRTEM) image (Figure 1e) of the hexagonal Cr_5Te_8 flake (Figure 1e inset) reveals a uniformly periodic

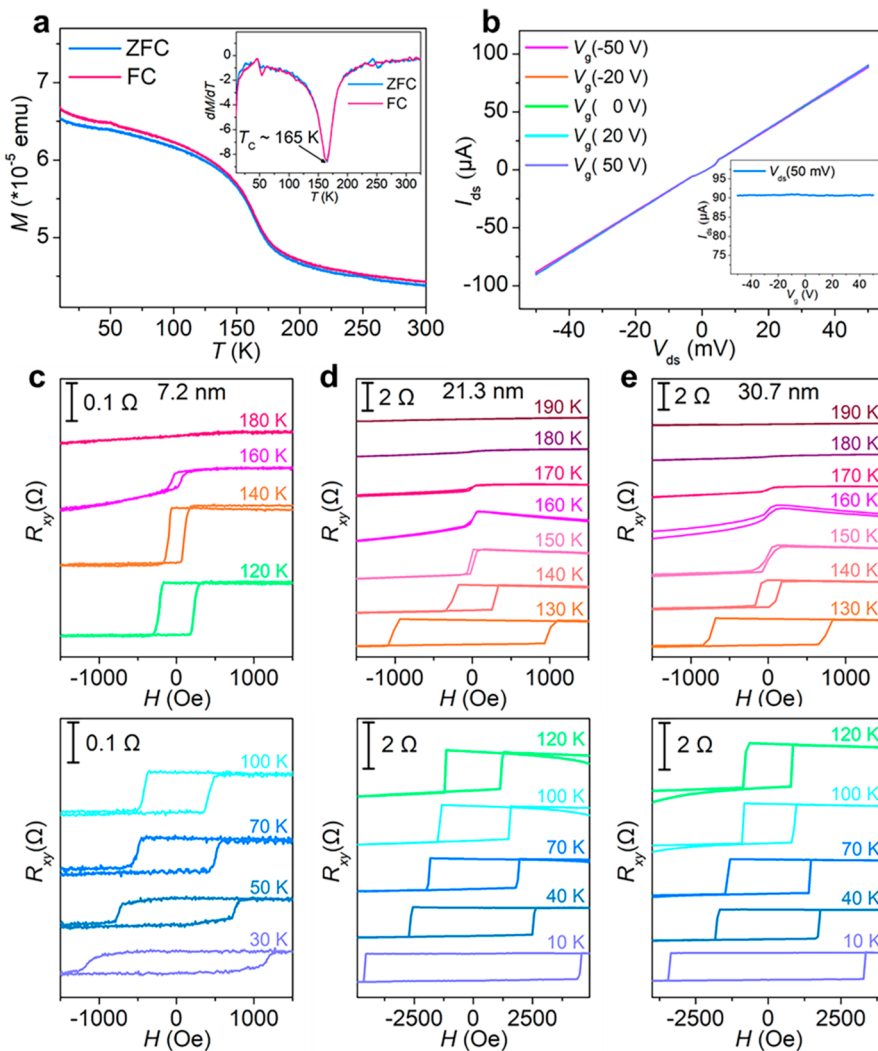


Figure 2. Electrical and magnetic characterizations of Cr_5Te_8 flakes. (a) Temperature-dependent magnetization of Cr_5Te_8 flakes grown on mica with the vertical magnetic field (along *c*-axis) at 0.4 T; the inset shows the derivative dM/dT curve. (b) I_{ds} – V_{ds} characteristics (V_g : −50 to +50 V) of 2D Cr_5Te_8 device. Inset shows transfer characteristics (V_{ds} : 50 mV) of Cr_5Te_8 device using the Si/SiO₂ substrate as a back gate. (c–e) Temperature-dependent Hall resistance hysteresis loops of 7.2 (c), 21.3 (d), and 30.7 (e) nm Cr_5Te_8 devices.

atom arrangement with lattices spacing of 0.197 nm, corresponding to the (220) planes of trigonal Cr_5Te_8 .³⁵ Furthermore, the corresponding selected area electron diffraction (SAED) pattern shows a single set of hexagonally arranged diffraction spots, revealing the hexagonal symmetry of the Cr_5Te_8 (Figure 1f). The (100) lattice plane spacing measured from Figure 1f is 0.679 nm, matching the standard PDF card (JCPDS 50-1153) of bulk Cr_5Te_8 . Diffraction patterns of several locations on the flake present similar hexagonal patterns with the same direction, confirming the single-crystal nature of the Cr_5Te_8 flake (Figure S4). Randomly chosen flakes with various thicknesses are identified as trigonal Cr_5Te_8 through TEM and SAED characterizations (Figure S5a–f). Moreover, the elemental analysis of as-grown flakes shows the atomic ratio of Cr and Te is approximately 1:1.62 (Figure S5g), consistent with the stoichiometric ratio of Cr_5Te_8 .

The atomically resolved STEM shows that each Cr atom (dim spots) is surrounded by six Te atoms (light spots), matching well with the top-view atomic model of trigonal Cr_5Te_8 (Figure 1g). Interestingly, we can distinguish two alternating Cr spots with different intensities by extracting the

intensity line along the yellow dashed square in Figure 1g. The two types of Cr spots correspond to the Cr atoms stacking mode with (strong) and without (weak) the interlayer Cr atom in the trigonal Cr_5Te_8 structure (Figure 1h). The distance of adjacent Cr spots with the same intensity is 7.8 Å, consistent with the in-plane lattice constant (*a* and *b*) of trigonal Cr_5Te_8 .³⁵ Furthermore, there are no discernible vacancies or atomic defects in the STEM image, suggesting the high quality of as-grown flakes.

X-ray diffraction (XRD) and Raman spectra are utilized to further verify the crystal structure of as-synthesized flakes. To avoid interference from mica (Figure S6), we transfer Cr_5Te_8 flakes to quartz substrate for XRD measurement. Three diffraction peaks located at 15.14°, 30.12°, and 62.04° are indexed to the (002), (004), and (008) diffraction planes of trigonal Cr_5Te_8 (JCPDS 50-1153) (Figure 1i). All of the legible diffraction peaks belong to the family planes, implying that the *c*-axis of Cr_5Te_8 flakes is perpendicular to the substrate. The sharp XRD diffraction patterns reveal the high crystal quality of as-grown Cr_5Te_8 . All diffraction peaks of 2D Cr_5Te_8 shift to a higher degree of 0.2–0.4° compared to the bulk Cr_5Te_8 . This phenomenon indicates that the lattice

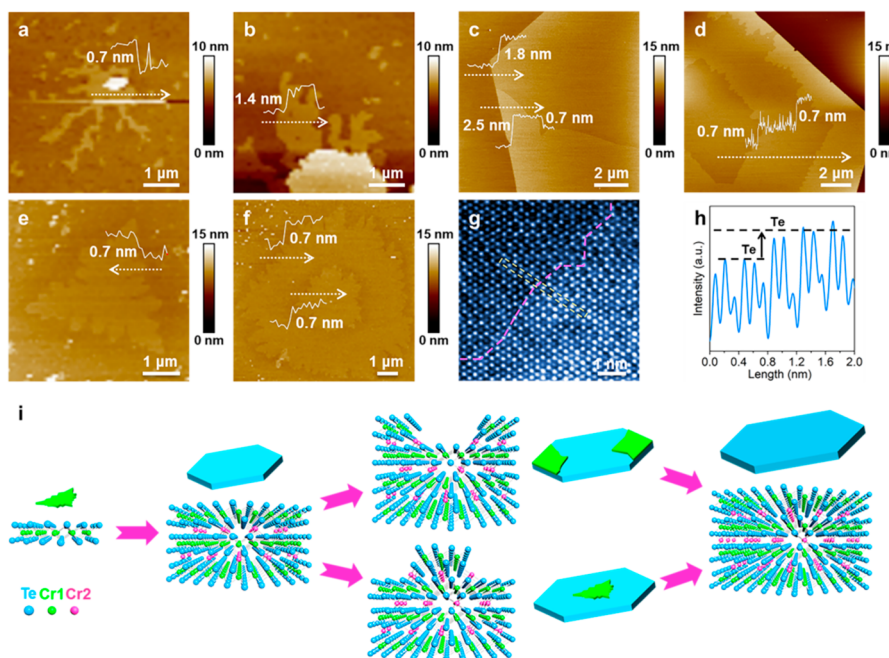


Figure 3. CVD growth mechanism of Cr₅Te₈ flakes. (a, b) AFM images of irregular flakes with 0.7 nm (a) and 1.4 nm (b) thick on mica. (c–f) AFM images of nanoflakes with sublayer growth on edge region (c, d) and central region (e, f). (g) HAADF-STEM image for the Cr₅Te₈ flake with a sublayer boundary. (h) Intensity line profile along the yellow dashed square in (g). (i) Schematic illustration of the growth process of 2D Cr₅Te₈ flakes. The green region denotes sublayer, while the blue area denotes Cr₅Te₈.

parameter along the *c*-axis gets smaller in the 2D limit, which also exists in other 2D material systems.³² We also compare the Raman spectra of as-synthesized 2D flake and bulk Cr₅Te₈ crystal (Figure 1j). Three prominent Raman peaks at 100.2, 124.3, and 139.7 cm⁻¹ appear for 2D Cr₅Te₈ flake, close to the Raman peaks (99.9, 124.0, and 140.4 cm⁻¹) of bulk Cr₅Te₈ crystal. All these characterizations results verify the as synthesized 2D flakes are high-quality trigonal Cr₅Te₈.

We further investigate the chemical stability of 2D Cr₅Te₈ flakes by comparing their morphology, structure, and electrical properties before and after treatment. After exposure to air for one month, the optical contrast of the Cr₅Te₈ flakes (4.3 and 16.6 nm) shows no noticeable change (Figure S7a–d). Moreover, AFM images show that the flake's morphology, thickness, and surface roughness (R_q) have no detectable change (Figure S7e–h). These results demonstrate the outstanding air stability of the materials. Structural characterizations of 2D Cr₅Te₈ flakes before and after exposure to the air for one month (Figure S8a–c) reveal that the flake remains intact and keep the single crystalline nature. The output characteristics of the Cr₅Te₈ device present a negligible change after one month (Figure S8d). The unchanged crystal structure and electrical property unequivocally indicate the high stability of 2D Cr₅Te₈ in air. Furthermore, the 2D Cr₅Te₈ flake exhibits good air stability after exposure to natural light for one month (Figure S9). The morphology of a single-unit-cell-thick Cr₅Te₈ has no distinct change after 1.5 years (Figure S10). We also investigate the thermal stability of 2D Cr₅Te₈ by annealing at 300 °C in Ar for 1 h. After the annealing treatment, optical contrast (Figure S11a,b), morphology (Figure S11a–d), thickness (Figure S11c,d), and surface roughness (Figure S11e–g) of the flake show no obvious change. These results demonstrate that 2D Cr₅Te₈ is stable at 300 °C in Ar. To further evaluate the stability of as-synthesized Cr₅Te₈ under extreme conditions, we treat 2D Cr₅Te₈ samples under harsh

conditions. The morphologies of the Cr₅Te₈ flakes are perfectly retained after treatment in concentrated HCl (38 wt %), H₂SO₄ (98 wt %), and saturated NaOH aqueous solution (52 wt %) for 10 min (Figure S12). These studies prove that the as-prepared Cr₅Te₈ flakes are robust both in ambient and harsh conditions.

We next probe the intrinsic magnetism of the as-synthesized Cr₅Te₈ flakes via the magnetic susceptibility measurement. As shown in Figure 2a, the magnetization of the randomly distributed Cr₅Te₈ samples with different thicknesses on the mica substrate under an applied vertical magnetic field of $H = 0.4$ T exhibits a magnetic phase transition at $T_c \sim 165$ K (inset of Figure 2a), which is lower than the reported ferromagnetism of the bulk trigonal Cr₅Te₈ crystal ($T_c \sim 220$ K) with an out-of-plane (along *c* axis) easy axis.³⁶

To further explore the thickness dependence of the magnetic properties of our CVD-grown Cr₅Te₈ flakes, devices with the Hall-bar geometry (Figure S13a) are fabricated for the magnetotransport measurements. The *I*–*V* characteristics of a typical Cr₅Te₈ (14.9 nm flake) device show that the current increases linearly with the bias voltage (Figure 2b). The two-probe resistance is 555.6 Ohm with no obvious change observed in our measured gate voltage range (inset of Figure 2b), suggesting that the thin Cr₅Te₈ flake is metallic and connected ohmically to the electrodes. The out-of-plane ferromagnetism of Cr₅Te₈ with the thickness varying from 7.2 to 52.1 nm is probed via the anomalous Hall effect (Figure 2c–e, Figure S13b and S13c). Clearly defined hysteresis loops of the Hall resistance R_{xy} are observed in all samples at low temperatures, corresponding to the solid ferromagnetic state of the Cr₅Te₈. The spin configuration's change near the coercive field is sharp, denoting a spin-flip transition in an Ising-type ferromagnet with the out-of-plane magnetic anisotropy.³⁷ The coercive field becomes smaller with increasing temperature. The hysteresis loop gradually diminishes at 160–180 K,

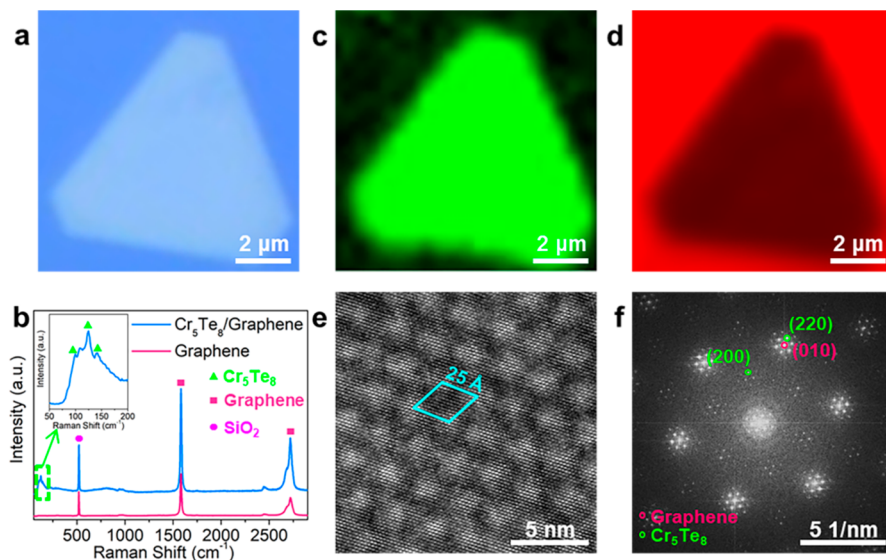


Figure 4. Characterizations of the Cr_5Te_8 /graphene heterostructure. (a) OM image of a vertical Cr_5Te_8 /graphene heterostructure (Cr_5Te_8 flake on graphene). (b) Raman spectra of graphene (peak intensity $\times 0.2$) and Cr_5Te_8 /graphene heterostructure. (c, d) Raman intensity maps of 124 cm^{-1} peak (c) and 1581 cm^{-1} peak (d) for the Cr_5Te_8 /graphene heterostructure. (e) HRTEM image of Cr_5Te_8 /graphene heterostructure with $\sim 25 \text{ \AA}$ period moiré pattern. (f) FFT image of atomic resolution HRTEM image in (e).

denoting a ferromagnetic to a paramagnetic phase transition, which is consistent with the magnetic susceptibility characterization (Figure 2a). Only slight changes of the Curie temperature (T_c) are observed from 52.1 to 7.2 nm, indicating that the magnetic coupling in the as-prepared Cr_5Te_8 is stable and robust, even when it approaches the 2D limit (4–5 unit cells).

The underlying mechanism of non-vdW materials to form ultimately thin 2D materials and the growth process play a vital role in understanding crystallization behavior and controlling morphologies of as-grown flakes. In contrast to vdW materials whose layer structure ensures lateral preferential growth, the intrinsic isotropic chemical bonds of non-vdW materials determine that synthesizing large-grain single-crystal 2D non-vdW materials is particularly difficult. We synthesize ultimately thin non-vdW Cr_5Te_8 with tens of micrometers and capture the growth process via AFM and STEM. Irregular sublayers with thicknesses of 0.7 nm (Figure 3a) and 1.4 nm (Figure 3b) occasionally form on the substrate. Sometimes we also find that one or two 0.7 nm sublayer randomly distribute on the surface of as-grown Cr_5Te_8 flakes (Figure 3c–f, Figure S14). The sublayer follows either outer-to-inner growth or inner-to-outer growth modes (Figure S14a–d). Multiple sublayer domains on Cr_5Te_8 flakes finally combine to form continuous layers (Figure S14e–h). STEM images visualize the atomic structure of both the sublayer on Cr_5Te_8 and the underlying Cr_5Te_8 flake. The boundary between these two regions is atomically smooth (Figure 3g,h).

Controlled experiments reveal that higher Cr amounts lead to thicker flakes and larger variations of thicknesses, while the lateral size of flakes has no obvious changes (Figure S15). Inspired by the layer-by-layer growth we observed and the self-intercalation growth mode in TaS_x ,³⁸ we suppose the growth in the vertical direction is strongly influenced by the concentration of metal source. In the metal source-rich environment, metal adatoms on the top layer of Cr_5Te_8 become nucleation sites of new sublayers.

Based on all these phenomena, we suppose the scenario of 2D non-vdW Cr_5Te_8 growth is “layer-by-layer growth” (Figure 3i). First, an irregular sublayer (possible CrTe_2) grows on the substrate. Second, Cr atoms adsorb on the sublayer. As Cr atoms accumulate and occupy all the octahedral vacancies between sublayers, the Cr adatoms initiate the formation of the top sublayer. Three CrTe_2 sublayers and two Cr atomic layers form a single unit cell Cr_5Te_8 . Third, as the growth proceeds, the single unit cell grows large, and sublayers randomly nucleate on Cr_5Te_8 surface. Fourth, the sublayers grow, merge, and completely cover the whole Cr_5Te_8 crystal. We infer that the growth of the Cr_5Te_8 flake and sublayer follow different growth modes. The fractal-like sublayer reveals the diffusion-limited growth mode. On the contrary, the Cr_5Te_8 crystal shows a hexagonal shape with straight edges, indicating the growth of Cr_5Te_8 flakes follows the attachment-limited growth mode.³⁹

Inspired by the large-grain atomically thin non-vdW and layer-by-layer growth, we directly grow 2D non-vdW materials on vdW materials via CVD. 2D Cr_5Te_8 flakes are grown on common 2D vdW materials, including graphene, h-BN, and MoS_2 . The Cr_5Te_8 flake on exfoliated graphene forms a vertical Cr_5Te_8 /graphene heterostructure with a uniform optical contrast (Figure 4a). Raman spectra of the Cr_5Te_8 /graphene heterostructure (blue curve in Figure 4b) show characteristic peaks from both Cr_5Te_8 and graphene, suggesting the Cr_5Te_8 and graphene are intact in the heterostructure. The location and uniformity of the heterostructure are further verified by Raman mapping. Raman intensity maps clearly distinguish the Cr_5Te_8 /graphene heterostructure region from the bare graphene region (Figure 4c,d). The homogeneous color of the heterostructure region in Figure 4c (A_{1g} peak of Cr_5Te_8) and Figure 4d (G peak of graphene) manifest that as-grown Cr_5Te_8 and underlying graphene are uniform in the heterostructure. Interestingly, multiple Cr_5Te_8 grains on a single graphene flake always show parallel edges (Figure S16a). This phenomenon reveals Cr_5Te_8 flakes on graphene have the same crystal orientations, suggesting a preferred epitaxial

relationship with graphene. Furthermore, we also characterize Cr₅Te₈/MoS₂ and Cr₅Te₈/h-BN heterostructures by optical microscopy (Figure S16c,d) and Raman spectroscopy (Figure S16e,f). These results confirm that we can integrate a 2D non-vdW ferromagnet with vdW materials and construct diverse non-vdW/vdW heterostructures.

A moiré superlattice is clearly displayed in real space for the Cr₅Te₈/graphene heterostructure through high-resolution TEM (Figure 4e). The superlattice has a well-defined moiré periodicity of ~2.5 nm. The corresponding FFT image (Figure 4f) presents two distinct sets of hexagonal patterns. The honeycomb pattern with lattice spacings of 0.214 nm corresponds to the (010) plane of graphene. The lattice spacings of 0.340 and 0.197 nm match well with the (100) and (220) planes of Cr₅Te₈, respectively. The (220) plane of Cr₅Te₈ aligns with the (010) plane of graphene and has no apparent rotation. The satellite peaks around the central beam spot suggest moiré superlattice originated from the interactions between Cr₅Te₈ and graphene layers.⁴⁰ We can calculate the periodicity using the formula

$$\lambda = \frac{(1 + \delta)\alpha}{\sqrt{2(1 + \delta)(1 - \cos \phi) + \delta^2}} \quad (1)$$

where λ is the period of moiré superlattice, α is the graphene's lattice constant, δ is the lattice mismatch between the (220) plane of Cr₅Te₈ and the (010) plane of graphene (here is 8.63%), and ϕ is the relative rotation angle between the two lattices (here is 0°).⁴¹ The calculated moiré periodicity is 2.48 nm, consistent with the periodicity measured in real space. Moreover, the superlattice is highly ordered without lattice distortion, revealing the high quality of the moiré superlattice. We also observed clear moiré superlattices in Cr₅Te₈/MoS₂ and Cr₅Te₈/h-BN heterostructures with periodicities of ~0.9 and 1.5 nm, respectively (Figure S17b,e).

CONCLUSIONS

In summary, we synthesize ultrathin magnetic Cr₅Te₈ flakes with tunable thickness and a magnetic moiré superlattice. The as-grown Cr₅Te₈ flakes exhibit high-quality single-crystalline structures. The grain sizes of single Cr₅Te₈ flakes are up to submillimeter, and the thinnest Cr₅Te₈ flake has a lateral size of about tens of micrometers. The Cr₅Te₈ flakes are robust both in harsh and ambient conditions after one month of exposure. The intrinsic stability mechanism of 2D Cr₅Te₈ (including single unit cell thick Cr₅Te₈) is intriguing and might inspire a direction of 2D magnets. Magnetotransport measurements reveal the 2D Cr₅Te₈ is ferromagnetic with an out-of-plane easy axis. Ferromagnetic properties of Cr₅Te₈ flakes with different thicknesses do not show obvious changes. We find that the growth of non-vdW Cr₅Te₈ follows the "layer-by-layer" mode. Based on the 2D non-vdW Cr₅Te₈, we construct diverse vertical heterostructures (Cr₅Te₈/graphene, Cr₅Te₈/h-BN, Cr₅Te₈/MoS₂). A highly ordered and uniformed moiré superlattice is formed in the heterostructure due to lattice mismatch. The scalable synthesis method for 2D non-vdW magnets and moiré superlattice offers a general avenue to fabricate 2D magnetic moiré superlattice.

METHODS

CVD Growth of Cr₅Te₈ Flakes. 2D Cr₅Te₈ flakes were grown on SiO₂/Si and mica substrates by the atmospheric pressure chemical vapor deposition. A 1-in. quartz tube was used and kept in a two-zone

furnace. Tellurium powder (Aldrich, 99.99%) was placed in a quartz boat, loaded upstream in the first zone. CrCl₂ powder (Strem Chemicals, 99.9%) and substrates were put in the second zone. The SiO₂/Si substrate and fresh-cleaved fluorophlogopite mica ([KMg₃(AlSi₃O₁₀)F₂]) were behind the CrCl₂ powder. Before the heating process, the quartz tube was preheated to ~200 °C. The CVD system was vacuumed and purged by Ar gas three times to remove water and air. Then the first and second zones simultaneously ramped up to 600 and 800 °C within 15 min. A 200 sccm Ar was used during the whole growth. We varied the growth time from 0 to 15 min to grow Cr₅Te₈ flakes with different thicknesses and domain sizes. After growth, the flux of the Ar gas was changed to 50 sccm. The quartz tube was taken out from the furnace and rapidly cooled to room temperature.

CVD Growth of Cr₅Te₈ Heterostructures. 2D graphene, MoS₂, and h-BN first prepared on the substrates (SiO₂/Si and mica) by mechanical exfoliation. Then Cr₅Te₈ flakes were directly grown on 2D graphene, MoS₂, and h-BN under the same conditions as CVD growth of Cr₅Te₈ flakes on SiO₂/Si and mica. The growth time was 0–1 min.

Characterization. The morphology and crystal structure of the 2D Cr₅Te₈ flakes were measured by optical microscope (OM, Leica DM2700M), X-ray diffraction (XRD, Mini Flex 600), Raman spectroscopy (Horiba xplora plus, 532 nm excitation laser), atomic force microscopy (AFM, Bruker Multimode 8), transmission electron microscopy (TEM, FEI Talos F200X), selected area electron diffraction (SAED), high-resolution transmission electron microscopy (HRTEM), and aberration-corrected scanning transmission electron microscopy (STEM, Nion U-HERME200).

Preparation of TEM and STEM Samples. The Cr₅Te₈ flakes grown on mica were transferred to TEM grids by poly(methyl methacrylate) (PMMA, Aldrich, MW ~ 35000)-assisted wet transfer process. The PMMA solution was spin-coated on the mica substrate with as-grown Cr₅Te₈ flakes at a speed of 3000 rpm for 60 s and then baked on a heating plate at 60 °C for 30 min. A PMMA film with some Cr₅Te₈ flakes was peeled off from the mica substrate by a tweezer with the assistance of water. Then a TEM grid is used to pick up the film. The TEM grid with PMMA film was heated at 60 °C for 10 h and then afterward immersed into acetone for 30 min to remove PMMA.

Device Fabrication, Electrical and Magnetic Measurements. The Hall-bar devices were fabricated on SiO₂/Si substrates by a laser direct writing lithography technique (DaLI-B, miDALIX) followed by electron beam evaporation of Ti/Au (4/40 nm) electrodes. The Cr₅Te₈ samples used in electrical and magnetic measurements were transferred to the Hall-bar electrodes via a dry transfer technique. Electrical measurements were carried out in a semiconductor parameter analyzer (Keithley 4200-SCS). Temperature-dependent magnetic susceptibility of samples on mica substrates was characterized using a superconducting quantum interference diffractometer (SQUID, Quantum Design MPMS3). The magnetotransport measurements were carried out in a physical property measurement system (Quantum Design PPMS-9T (EC-II)). The longitudinal resistance (R_{xx}) and Hall resistance (R_{xy}) were measured by passing a constant ac bias current of 20 μA ($f = 13.4$ Hz) through the device and recording the electrical potential difference between corresponding voltage probes using digital lock-in amplifiers (Stanford Research; SR830). The temperature and the magnetic field were tuned by the PPMS.

ASSOCIATED CONTENT

Supporting Information

The Supporting Information is available free of charge at <https://pubs.acs.org/doi/10.1021/acsnano.1c11018>.

OM and AFM images of Cr₅Te₈ flakes; TEM images, SAED patterns and EDS elemental analysis of Cr₅Te₈ flakes; XRD of 2D Cr₅Te₈ flakes on mica and bare mica; characterization data (OM images, AFM images, TEM

image, HRTEM image, SAED pattern, and I_{ds} – V_{ds} curve of a Cr_5Te_8 device) for the stability of Cr_5Te_8 flakes; OM images of Cr_5Te_8 device, temperature-dependent Hall resistance hysteresis loops of 14.6 and 52.1 nm Cr_5Te_8 devices; controlled experiments of Cr amount; OM and TEM image of Cr_5Te_8 /graphene heterostructure; OM images, Raman spectra, TEM images, HRTEM images, and SAED patterns of $\text{Cr}_5\text{Te}_8/\text{MoS}_2$ and $\text{Cr}_5\text{Te}_8/\text{h-BN}$ heterostructures (PDF)

AUTHOR INFORMATION

Corresponding Authors

Lin Zhou – School of Chemistry and Chemical Engineering, Frontiers Science Centre for Transformative Molecules, Shanghai Jiao Tong University, Shanghai 200240, China; orcid.org/0000-0001-7969-3839; Email: linzhou@sjtu.edu.cn

Xinghan Cai – National Key Laboratory of Science and Technology on Micro/Nano Fabrication, Department of Micro/Nano Electronics, School of Electronic Information and Electrical Engineering, Shanghai Jiao Tong University, Shanghai 200240, China; orcid.org/0000-0002-9274-2444; Email: xhcai@sjtu.edu.cn

Authors

Zhitong Jin – School of Chemistry and Chemical Engineering, Frontiers Science Centre for Transformative Molecules, Shanghai Jiao Tong University, Shanghai 200240, China

Zijie Ji – National Key Laboratory of Science and Technology on Micro/Nano Fabrication, Department of Micro/Nano Electronics, School of Electronic Information and Electrical Engineering, Shanghai Jiao Tong University, Shanghai 200240, China

Yunlei Zhong – School of Chemistry and Chemical Engineering, Frontiers Science Centre for Transformative Molecules, Shanghai Jiao Tong University, Shanghai 200240, China

Yunmin Jin – National Key Laboratory of Science and Technology on Micro/Nano Fabrication, Department of Micro/Nano Electronics, School of Electronic Information and Electrical Engineering, Shanghai Jiao Tong University, Shanghai 200240, China

Xianyu Hu – School of Chemistry and Chemical Engineering, Frontiers Science Centre for Transformative Molecules, Shanghai Jiao Tong University, Shanghai 200240, China

Xingxing Zhang – School of Chemistry and Chemical Engineering, Frontiers Science Centre for Transformative Molecules, Shanghai Jiao Tong University, Shanghai 200240, China

Lijing Zhu – School of Chemistry and Chemical Engineering, Frontiers Science Centre for Transformative Molecules, Shanghai Jiao Tong University, Shanghai 200240, China

Xianhui Huang – School of Chemistry and Chemical Engineering, Frontiers Science Centre for Transformative Molecules, Shanghai Key Laboratory of Electrical Insulation and Thermal Aging, Shanghai Jiao Tong University, Shanghai 200240, China

Tao Li – School of Chemistry and Chemical Engineering, Frontiers Science Centre for Transformative Molecules, Shanghai Key Laboratory of Electrical Insulation and Thermal Aging, Shanghai Jiao Tong University, Shanghai 200240, China; orcid.org/0000-0002-2410-0175

Complete contact information is available at:
<https://pubs.acs.org/10.1021/acsnano.1c11018>

Author Contributions

[‡]Z.J. and Z.J. contributed equally.

Notes

The authors declare no competing financial interest.

ACKNOWLEDGMENTS

This work was supported by National Key Basic R&D Program of China (2021YFA1401400 and 2020YFA0309200), the start-up funds of Shanghai Jiao Tong University, the National Natural Science Foundation of China (52103344, 92064013, 11904226, 22022507, and 51973111), and Beijing National Laboratory for Molecular Sciences (BNLMS202004). The authors acknowledge Weijun Ren and Teng Yang from the Institute of Metal Research, Chinese Academy of Sciences, for providing bulk Cr_5Te_8 crystals. The authors acknowledge the support of the miDALIX d.o.o for Hall-bar device fabrication.

REFERENCES

- (1) Andrei, E. Y.; MacDonald, A. H. Graphene Bilayers with a Twist. *Nat. Mater.* **2020**, *19*, 1265–1275.
- (2) Kennes, D. M.; Claessen, M.; Xian, L.; Georges, A.; Millis, A. J.; Hone, J.; Dean, C. R.; Basov, D. N.; Pasupathy, A. N.; Rubio, A. Moiré Heterostructures as a Condensed-Matter Quantum Simulator. *Nat. Phys.* **2021**, *17*, 155–163.
- (3) Balents, L.; Dean, C. R.; Efetov, D. K.; Young, A. F. Superconductivity and Strong Correlations in Moiré Flat Bands. *Nat. Phys.* **2020**, *16*, 725–733.
- (4) Andrei, E. Y.; Efetov, D. K.; Jarillo-Herrero, P.; MacDonald, A. H.; Mak, K. F.; Senthil, T.; Tutuc, E.; Yazdani, A.; Young, A. F. The Marvels of Moiré Materials. *Nat. Rev. Mater.* **2021**, *6*, 201–206.
- (5) Cao, Y.; Fatemi, V.; Fang, S.; Watanabe, K.; Taniguchi, T.; Kaxiras, E.; Jarillo-Herrero, P. Unconventional Superconductivity in Magic-Angle Graphene Superlattices. *Nature* **2018**, *556*, 43–50.
- (6) Cao, Y.; Fatemi, V.; Demir, A.; Fang, S.; Tomarken, S. L.; Luo, J. Y.; Sanchez-Yamagishi, J. D.; Watanabe, K.; Taniguchi, T.; Kaxiras, E.; Ashoori, R. C.; Jarillo-Herrero, P. Correlated Insulator Behaviour at Half-Filling in Magic-Angle Graphene Superlattices. *Nature* **2018**, *556*, 80–84.
- (7) Geisenhof, F. R.; Winterer, F.; Seiler, A. M.; Lenz, J.; Xu, T.; Zhang, F.; Weitz, R. T. Quantum Anomalous Hall Octet Driven by Orbital Magnetism in Bilayer Graphene. *Nature* **2021**, *598*, 53–58.
- (8) Jin, C.; Regan, E. C.; Yan, A.; Iqbal Bakti Utama, M.; Wang, D.; Zhao, S.; Qin, Y.; Yang, S.; Zheng, Z.; Shi, S.; Watanabe, K.; Taniguchi, T.; Tongay, S.; Zettl, A.; Wang, F. Observation of Moiré Excitons in WSe_2/WS_2 Heterostructure Superlattices. *Nature* **2019**, *567*, 76–80.
- (9) Regan, E. C.; Wang, D.; Jin, C.; Bakti Utama, M. I.; Gao, B.; Wei, X.; Zhao, S.; Zhao, W.; Zhang, Z.; Yumigeta, K.; Blei, M.; Carlstrom, J. D.; Watanabe, K.; Taniguchi, T.; Tongay, S.; Crommie, M.; Zettl, A.; Wang, F. Mott and Generalized Wigner Crystal States in WSe_2/WS_2 Moiré Superlattices. *Nature* **2020**, *579*, 359–363.
- (10) Tong, Q.; Liu, F.; Xiao, J.; Yao, W. Skyrmions in the Moiré of van der Waals 2D Magnets. *Nano Lett.* **2018**, *18*, 7194–7199.
- (11) Wang, C.; Gao, Y.; Lv, H.; Xu, X.; Xiao, D. Stacking Domain Wall Magnons in Twisted van der Waals Magnets. *Phys. Rev. Lett.* **2020**, *125*, 247201.
- (12) Hejazi, K.; Luo, Z. X.; Balents, L. Noncollinear Phases in Moiré Magnets. *Proc. Natl. Acad. Sci. U. S. A.* **2020**, *117*, 10721–10726.
- (13) Song, T.; Sun, Q.-C.; Anderson, E.; Wang, C.; Qian, J.; Taniguchi, T.; Watanabe, K.; McGuire, M. A.; Stöhr, R.; Xiao, D.; Cao, T.; Wrachtrup, J.; Xu, X. Direct Visualization of Magnetic Domains and Moiré Magnetism in Twisted 2D Magnets. *Science* **2021**, *374*, 1140–1144.

- (14) Li, B.; Wan, Z.; Wang, C.; Chen, P.; Huang, B.; Cheng, X.; Qian, Q.; Li, J.; Zhang, Z.; Sun, G.; Zhao, B.; Ma, H.; Wu, R.; Wei, Z.; Liu, Y.; Liao, L.; Ye, Y.; Huang, Y.; Xu, X.; Duan, X.; Ji, W.; Duan, X. Van der Waals Epitaxial Growth of Air-Stable CrSe₂ Nanosheets with Thickness-Tunable Magnetic Order. *Nat. Mater.* **2021**, *20*, 818–825.
- (15) Gong, C.; Li, L.; Li, Z.; Ji, H.; Stern, A.; Xia, Y.; Cao, T.; Bao, W.; Wang, C.; Wang, Y.; Qiu, Z. Q.; Cava, R. J.; Louie, S. G.; Xia, J.; Zhang, X. Discovery of Intrinsic Ferromagnetism in Two-Dimensional van der Waals Crystals. *Nature* **2017**, *546*, 265–269.
- (16) Huang, B.; Clark, G.; Navarro-Moratalla, E.; Klein, D. R.; Cheng, R.; Seyler, K. L.; Zhong, D.; Schmidgall, E.; McGuire, M. A.; Cobden, D. H.; Yao, W.; Xiao, D.; Jarillo-Herrero, P.; Xu, X. Layer-Dependent Ferromagnetism in a van der Waals Crystal down to the Monolayer Limit. *Nature* **2017**, *546*, 270–273.
- (17) Deng, Y.; Yu, Y.; Song, Y.; Zhang, J.; Wang, N. Z.; Sun, Z.; Yi, Y.; Wu, Y. Z.; Wu, S.; Zhu, J.; Wang, J.; Chen, X. H.; Zhang, Y. Gate-Tunable Room-Temperature Ferromagnetism in Two-Dimensional Fe₃GeTe₂. *Nature* **2018**, *563*, 94–99.
- (18) Chen, W.; Sun, Z.; Wang, Z.; Gu, L.; Xu, X.; Wu, S.; Gao, C. Direct Observation of van der Waals Stacking Dependent Interlayer Magnetism. *Science* **2019**, *366*, 983–987.
- (19) Deng, Y.; Yu, Y.; Shi, M. Z.; Guo, Z.; Xu, Z.; Wang, J.; Chen, X. H.; Zhang, Y. Quantum Anomalous Hall Effect in Intrinsic Magnetic Topological Insulator MnBi₂Te₄. *Science* **2020**, *367*, 895–900.
- (20) Burch, K. S.; Mandrus, D.; Park, J. G. Magnetism in Two-Dimensional van der Waals Materials. *Nature* **2018**, *563*, 47–52.
- (21) Gong, C.; Zhang, X. Two-Dimensional Magnetic Crystals and Emergent Heterostructure Devices. *Science* **2019**, *363*, No. eaav4450.
- (22) Mounet, N.; Gibertini, M.; Schwaller, P.; Campi, D.; Merkys, A.; Marrazzo, A.; Solier, T.; Castelli, I. E.; Cepellotti, A.; Pizzi, G.; Marzari, N. Two-Dimensional Materials from High-Throughput Computational Exfoliation of Experimentally Known Compounds. *Nat. Nanotechnol.* **2018**, *13*, 246–252.
- (23) Bonilla, M.; Kolekar, S.; Ma, Y.; Diaz, H. C.; Kalappattil, V.; Das, R.; Eggers, T.; Gutierrez, H. R.; Phan, M. H.; Batzill, M. Strong Room-Temperature Ferromagnetism in VSe₂ Monolayers on van der Waals Substrates. *Nat. Nanotechnol.* **2018**, *13*, 289–293.
- (24) Li, J.; Zhao, B.; Chen, P.; Wu, R.; Li, B.; Xia, Q.; Guo, G.; Luo, J.; Zang, K.; Zhang, Z.; Ma, H.; Sun, G.; Duan, X.; Duan, X. Synthesis of Ultrathin Metallic MTe₂ (M = V, Nb, Ta) Single-Crystalline Nanoplates. *Adv. Mater.* **2018**, *30*, 1801043.
- (25) Meng, L.; Zhou, Z.; Xu, M.; Yang, S.; Si, K.; Liu, L.; Wang, X.; Jiang, H.; Li, B.; Qin, P.; Zhang, P.; Wang, J.; Liu, Z.; Tang, P.; Ye, Y.; Zhou, W.; Bao, L.; Gao, H. J.; Gong, Y. Anomalous Thickness Dependence of Curie Temperature in Air-Stable Two-Dimensional Ferromagnetic 1T-CrTe₂ Grown by Chemical Vapor Deposition. *Nat. Commun.* **2021**, *12*, 809.
- (26) Chen, S.; Liu, H.; Chen, F.; Zhou, K.; Xue, Y. Synthesis, Transfer, and Properties of Layered FeTe₂ Nanocrystals. *ACS Nano* **2020**, *14*, 11473–11481.
- (27) Liu, H.; Xue, Y. Van Der Waals Epitaxial Growth and Phase Transition of Layered FeSe₂ Nanocrystals. *Adv. Mater.* **2021**, *33*, 2008456.
- (28) Jin, C.; Kou, L. Two-dimensional non-van der Waals Magnetic Layers: Functional Materials for Potential Device Applications. *J. Phys. D: Appl. Phys.* **2021**, *54*, 413001.
- (29) Zhou, S.; Wang, R.; Han, J.; Wang, D.; Li, H.; Gan, L.; Zhai, T. Ultrathin Non-van der Waals Magnetic Rhombohedral Cr₂S₃: Space-Confining Chemical Vapor Deposition Synthesis and Raman Scattering Investigation. *Adv. Funct. Mater.* **2019**, *29*, 1805880.
- (30) Zhang, Y.; Chu, J.; Yin, L.; Shifa, T. A.; Cheng, Z.; Cheng, R.; Wang, F.; Wen, Y.; Zhan, X.; Wang, Z.; He, J. Ultrathin Magnetic 2D Single-Crystal CrSe. *Adv. Mater.* **2019**, *31*, 1900056.
- (31) Kang, L.; Ye, C.; Zhao, X.; Zhou, X.; Hu, J.; Li, Q.; Liu, D.; Das, C. M.; Yang, J.; Hu, D.; Chen, J.; Cao, X.; Zhang, Y.; Xu, M.; Di, J.; Tian, D.; Song, P.; Kutty, G.; Zeng, Q.; Fu, Q.; Deng, Y.; Zhou, J.; Ariando, A.; Miao, F.; Hong, G.; Huang, Y.; Pennycook, S. J.; Yong, K. T.; Ji, W.; Wang, X. R.; Liu, Z. Phase-Controllable Growth of Ultrathin 2D Magnetic FeTe Crystals. *Nat. Commun.* **2020**, *11*, 3729.
- (32) Wen, Y.; Liu, Z.; Zhang, Y.; Xia, C.; Zhai, B.; Zhang, X.; Zhai, G.; Shen, C.; He, P.; Cheng, R.; Yin, L.; Yao, Y.; Sendeku, M. G.; Wang, Z.; Ye, X.; Liu, C.; Jiang, C.; Shan, C.; Long, Y.; He, J. Tunable Room-Temperature Ferromagnetism in Two-Dimensional Cr₂Te₃. *Nano Lett.* **2020**, *20*, 3130–3139.
- (33) Chen, C.; Chen, X.; Wu, C.; Wang, X.; Ping, Y.; Wei, X.; Zhou, X.; Lu, J.; Zhu, L.; Zhou, J.; Zhai, T.; Han, J.; Xu, H. Air-Stable 2D Cr₅Te₈ Nanosheets with Thickness-Tunable Ferromagnetism. *Adv. Mater.* **2022**, *34*, 2107512.
- (34) Ipser, H.; Komarek, K. L. Transition Metal-Chalcogen Systems VIII—the Cr-Te Phase Diagram. *J. Less-Common Met.* **1983**, *92*, 265–282.
- (35) Bensch, W.; Helmer, O.; Näther, C. Determination and Redetermination of the Crystal Structures of Chromium Tellurides in the Composition Range CrTe_{1.56}–CrTe_{1.67}: Trigonal Di-Chromium Tri-Telluride Cr₂Te₃, Monoclinic Penta-Chromium Octa-Telluride Cr₅Te₈, and the Five Layer Superstructure of Trigonal Penta-Chromium Octa-Telluride Cr₅Te₈. *Mater. Res. Bull.* **1997**, *32*, 305–318.
- (36) Shimada, T. S. K.; Namatame, H.; Fujimori, A. Photoemission Study of Itinerant Ferromagnet Cr_{1-δ}Te. *Phys. Rev. B* **1996**, *53*, 7673–7683.
- (37) Liu, Y.; Petrovic, C. Critical Behavior of the Quasi-Two-Dimensional Weak Itinerant Ferromagnet Trigonal Chromium Telluride Cr_{0.62}Te. *Phys. Rev. B* **2017**, *96*, 134410.
- (38) Zhao, X.; Song, P.; Wang, C.; Riis-Jensen, A. C.; Fu, W.; Deng, Y.; Wan, D.; Kang, L.; Ning, S.; Dan, J.; Venkatesan, T.; Liu, Z.; Zhou, W.; Thygesen, K. S.; Luo, X.; Pennycook, S. J.; Loh, K. P. Engineering Covalently Bonded 2D Layered Materials by Self-Intercalation. *Nature* **2020**, *581*, 171–177.
- (39) Dong, J.; Zhang, L.; Ding, F. Kinetics of Graphene and 2D Materials Growth. *Adv. Mater.* **2019**, *31*, 1801583.
- (40) Reidy, K.; Varnavides, G.; Thomsen, J. D.; Kumar, A.; Pham, T.; Blackburn, A. M.; Anikeeva, P.; Narang, P.; LeBeau, J. M.; Ross, F. M. Direct Imaging and Electronic Structure Modulation of Moiré Superlattices at the 2D/3D Interface. *Nat. Commun.* **2021**, *12*, 1290.
- (41) Yankowitz, M.; Xue, J.; Cormode, D.; Sanchez-Yamagishi, J. D.; Watanabe, K.; Taniguchi, T.; Jarillo-Herrero, P.; Jacquod, P.; LeRoy, B. J. Emergence of Superlattice Dirac Points in Graphene on Hexagonal Boron Nitride. *Nat. Phys.* **2012**, *8*, 382–386.